Scientific Article

Model evaluation of rapid 4-dimensional lung tomosynthesis

Joseph T. Rakowski PhD *

Karmanos Cancer Institute, Wayne State University School of Medicine, Department of Oncology, Division of Radiation Oncology, Detroit, Michigan

Abstract

Purpose: This is an investigation of a lung motion digital tomosynthesis (DTS) model using combined stationary detector and stationary cold cathode x-ray sources at projection acquisition rates that exceed the present norms. The intent is to reduce anatomical uncertainties from artifacts inherent in thoracic 4-dimensional computed tomography (CT).

Methods and materials: Parameters necessary to perform rapid lung 4-dimensional DTS were studied using a conventional radiographic system with linear motion of the x-ray source and a simple hypothetical hardware performance model. Hypothetical rapid imaging parameters of sweep duration, projections per second, pulse duration, and tube current (mA) were derived on the basis of 0.5 mm and 1 mm motion captures per phase, 10 and 15 breaths per minute (bpm), 10 to 40 mm breathing amplitude, and 2 signal-to-noise ratio (SNR) levels. Anterior-posterior and lateral projection images of a normal size anthropomorphic thorax phantom with iodine contrast inserts were collected and reconstructed with an algebraic algorithm to study the effects of reduced x-ray output associated with field emission cold cathodes composed of carbon nanotubes or metal Spindt-type. Radiographic projections were collected at 3 SNR levels that were set at standard clinical DTS milliampere-seconds (mAs) and reduced corresponding to 50% and 25% standard DTS mAs to simulate a reduced x-ray output.

Results: The DTS SNR of the inserts was superior in all reconstructions at clinical mAs versus automatic exposure-control radiographs and superior in 3 of 4 at the 50% and 25% mAs levels. The most demanding performance parameters corresponding to 40 mm amplitude, 15 bpm, 0.5 mm motion capture limit, and 61 projections were sweep duration (10.4 msec), projection rate (5862 projections per second), pulse duration (0.161 msec), current 189 mA anterior-posterior, and 653 mA lateral.

Conclusions: Feasibility depends on the output performance of stationary cold cathode hardware being developed for DTS. Present image receptor technology can accommodate frame acquisition rates.

© 2018 The Author(s). Published by Elsevier Inc. on behalf of the American Society for Radiation Oncology. This is an open access article under the CC BY-NC-ND license (http://creativecommons.org/licenses/by-nc-nd/4.0/).

Introduction

Stereotactic body radiation therapy (SBRT) requires accurate delineation of the internal target volume. Lung SBRT simulation involves 4-dimensional computed tomography

(CT), often with iodine contrast administered. The advantage of 4-dimensional CT is the target localization during respiration, assuming the simulation breathing pattern is repeated during treatment. There are several approaches for performing 4-dimensional CT to this end: helical or cine, prospectively or retrospectively, with amplitude-based or phase-based reconstruction.[1] Four-dimensional CT is often accompanied by artifacts that can be grouped into 4 types: blurring, duplicate structure, overlapping structure, and incomplete structure.[2] Intrinsic causes are organ motion exceeding the temporal resolution of the scanner and changes in respiration rate or amplitude over the course of a complete scan wherein the body is imaged in sections over several breathing cycles that encompass irregular respiration.

Lung digital tomosynthesis (DTS) has been investigated as a modality for pulmonary nodule detection and management.[3] However, nodules are not necessarily indicative of cancer and play no role in SBRT target delineation.[4-6] The application of DTS to nodule detection lends support to inclusion in treatment planning. Investigations into stationary x-ray sources for gated chest DTS were conducted at the University of North Carolina at Chapel Hill.[7-9] Shan et al focused on prospective gated chest DTS using stationary carbon nanotube x-ray sources.[9] Their study captured 10 breaths per minute (bpm), end of exhalation images at 30 projections per second (pps), 80 kVp, 5 mA anode current, 25 and 50 milliseconds per projection pulse, and 5 projections per respiration cycle with the whole sequence requiring 36 seconds across 6 respiration cycles.

Studies have been published on radiation therapy guidance DTS. Maurer et al proposed linac on-board 4-dimensional DTS using respiratory-correlated cone beam CT projections and found greater craniocaudal motion artifact suppression relative to 4-dimensional CT.[10] Hsieh and Ng proposed linac gantry-mounted DTS to provide real-time guidance at up to 30 frames per second.[11] Zhang et al proposed lung localization during linac radiation therapy via DTS reconstructions from 4-dimensional CT simulation, phase-matched, digitally reconstructed radiographs and DTS images from cone beam CT collected at treatment.[12] Zhang et al later published a phase-matched, orthogonal-view, retrospective study that showed a tumor localization average error of 1.8 ± 0.7 mm and a phantom study error within 1 mm.[13] Santoro et al compared linac on-board imaging respiration-correlated DTS from cone beam CT projections with respiration-correlated cone beam CT to determine tumor position, motion extent, and displacement between treatment sessions and found agreement, in most cases within 2 to 3 mm.[14] Maltz et al published a fixed-gantry DTS guidance system using a multisource x-ray tube with carbon nanotube cathodes.[15]

Rapid 4-dimensional DTS in SBRT planning requires capture of multiple phases over a single breathing cycle. This paper explores the performance requirements using multiphase or multiamplitude capture with constraints on allowable lung tissue displacement per phase. Rapid 4-dimensional DTS offers the advantages of capturing full craniocaudal and lateral extent in the coronal projections, plus the full anterior-posterior (AP) extent in sagittal projections, with a user-selected maximum range of craniocaudal motion within each phase, which was selected here as 0.5 and 1 mm. Capturing all phases and anatomy in a single breathing cycle preserves the spatiotemporal integrity of tissue, which can be compromised in multicycle, slow 4-dimensional DTS and provides a direct link between lung and diaphragm motion.

In 4-dimensional CT, amplitude and rate variations coupled with scan volume limitations leads to artifacts. For example, inhalation rate or amplitude may vary between different sections of the lung in the craniocaudal direction as the z-limited beam passes over. Lung hysteresis is affected by differences in breathing amplitudes and rates, all of which are patient specific and variable, making tumor motion prediction difficult.[16] The working premise in rapid 4-dimensional DTS is that spatiotemporal uncertainties in 4-dimensional CT can be reduced or eliminated by single-cycle imaging of the entire lung, provided the patient can perform a single good breathing cycle.

Rapid 4-dimensional DTS will limit motion artifacts and provide high resolution in the coronal and sagittal reconstruction planes. Spatial resolution in the reconstruction plane will depend on geometric blur and flat-panel detector dexel pitch. In-plane resolution in the coronal and sagittal planes can facilitate precise target segmentation. The approximate 1 cm slice thickness inherent in DTS can be compensated by orthogonal projections, with Boolean merger of segmentations from orthogonal image sets compensating for lower resolution in the orthogonal depth direction.[13] Four-dimensional CT will continue to provide curvilinear contour accuracy in the axial plane, complemented by rapid 4-dimensional DTS. Target conspicuity may be enhanced through intravenous iodine contrast as administered for 4-dimensional CT.[17]

Operation of this model would entail 61 projections through a linear sweep angle $\geq 40°$. The sources configuration and sweep orientation can be 2-dimensional and the number of projections negotiable.[11,15] Sweep refers to the sequential firing of all focal spots during the collection of a complete set of tomographic projections at a given single breathing phase. A larger number of projections minimizes the ripple artifact, and a greater sweep angle improves depth resolution.[18] Tube current milliampere-seconds (mAs) per projection over a single arc are a fraction of the mAs required for a conventional radiograph.[19] Projections per second per phase is set to limit the captured motion during any phase to a predefined limit. Heart motion artifacts may be reduced by simultaneous cardiac gating with imaging that is performed during the quiescence, although this would extend imaging beyond a single breathing cycle. Digital Imaging and Communications in Medicine coordinate

system sharing by physical link between the CT and 4-dimensional DTS system will allow coregistration of 4-dimensional DTS and 4-dimensional CT, with lesion selection in the CT image set determining the target of 4-dimensional DTS reconstruction and lesion delineation. Four-dimensional CT will continue as the primary modality and provide axial curvilinear contouring accuracy.

Stationary sources rapid exposures are provided by cold cathode carbon nanotube field emission or higher output Spindt-type metal field emission cathodes.[20-23] High frame rates will not challenge the x-ray emitter repetition rate because each will fire once per sweep, with 10 or fewer sweeps over a breathing cycle. The frame rate will challenge image receptor and readout systems but is within the limits of available imaging systems (Radiation Monitoring Devices, Inc., Watertown, MA).

Methods and materials

Four-dimensional tomosynthesis model

Tomosynthesis projection pps adequate for limiting craniocaudal motion to a predetermined distance during capture of an individual phase depends on the following:

1) Motion amplitude b
2) The desired maximum tissue travel during the sweep D;
3) The number of projections per sweep NP; and
4) Phase-dependent tissue velocity.

Image quality depends on the number of projections, sweep angle, and mAs per projection.

Lujan et al describe the following breathing motion model:

$$z(t) = z_0 - b \times \cos^{2n}\left(\frac{\pi t}{\tau} - \varnothing_0\right), \qquad (1)$$

where $z(t)$ is craniocaudal position at time t; z_0 is the position at exhale; b is the amplitude of motion; $z_0 - b$ is the position at inhale; τ is the period of the breathing cycle; n is the parameter determining the waveform steepness and flatness; and $\varnothing_0$ is the starting phase of the breathing cycle.[24]

The instantaneous velocity at time t is:

$$\frac{dz(t)}{dt} = \frac{2n\pi b}{\tau} \cos^{2n-1}\left(\frac{\pi t}{\tau}\right) \sin\left(\frac{\pi t}{\tau}\right). \qquad (2)$$

The sweep duration per phase depends on the velocity at which the collection is performed. The required duration of a sweep at time t_A can be computed as:

$$Sweep\ Duration\,(t_A) = \left[D \Big/ \left(\frac{dz(t)}{dt}\right) \right]_{t_A}, \qquad (3)$$

where t_A is the midpoint time of image acquisition, $t_A = \frac{\tau}{\pi}(\varnothing_A + \varnothing_0)$, and $\varnothing_A$ is the breathing phase at acquisition. Time duration of acquisition extends from

$$t_A - \left[D \Big/ \left(\frac{dz(t)}{dt}\right) \right]_{t_A} \tau o\ t_A + \left[D \Big/ \left(\frac{dz(t)}{dt}\right) \right]_{t_A}. \qquad (4)$$

Craniocaudal lung tissue velocity is greatest, and sweep duration least, midway between maximum inhalation and maximum exhalation, in which:

$$\cos^{2n}\left(\frac{\pi t}{\tau} - \varnothing\right) = 0.5. \qquad (5)$$

The required pps at time t can be computed as:

$$Frame\ Rate = NP \big/ Sweep\ Duration. \qquad (6)$$

mAs per projection is

$$mAs\ per\ Projection = \frac{(mAs_{AEC}) \times f}{NP}. \qquad (7)$$

where mAs_{AEC} is the mAs per single radiographic exposure as determined by the automatic exposure control, and f is a noise-scaling factor with 10 regarded as clinically acceptable.[19]

$$Pulse\ Duration = \left(\frac{1}{frame\ rate}\right) - frame\ gap, \qquad (8)$$

where frame gap is the time duration between consecutive projections,

$$Frame\ Gap = \left(\frac{1}{100,000\ fps}\right) = 0.01\ msec, \qquad (9)$$

the 100,000 pps basis for the frame gap is short of the maximum available rate for radiographic imaging of 150,000 pps (Radiation Monitoring Devices, Inc.) and

$$mA = \frac{mAs\ per\ projection}{Pulse\ Duration}. \qquad (10)$$

Imaging system

The GE Brivo XR385 digital radiographic imaging system with stationary Gd_2O_2S:Tb receptor, 16 bits per pixel, 2022×2022 matrix, $38.42 \times 38.42\ cm^2$ (GE Healthcare, Aurora, OH) was used. The grid ratio is 13:1 and 70 lines/cm. The source-detector distance is 110 cm at 0° projection.

Phantom

The Kyoto Kagaku Chest Phantom N1 (Kyoto Kagaku, Torrance, CA) was used in this study. Iodine-infused lesions

were simulated with microcentrifuge tubes of 1.5 mL volume, 10 mm inner diameter, and a ratio of 30:1 solution of water to Omnipaque (GE Healthcare, Aurora, OH) contrast media for a predilution concentration of 350 mg/mL. The ratio was based on a prescribed injection of 70 mL at 3 mL/sec and cardiovascular output of 5000 mL/min:

$$\frac{\left(\dfrac{5000\ mL}{min}\right) \times \left(\dfrac{1\ min}{60\ sec}\right) \times \left(\dfrac{70\ mL}{3\ mL/sec}\right)}{70\ mL} = 27.8 \approx 30 \quad (11)$$

The tubes were positioned in the right and left lung posterior to the heart.

Projection imaging

To simulate a cold cathode emitter, focal spot linear array, the x-ray tube was translated along the craniocaudal direction. The tube angle was adjusted at each projection so that the central ray extended from the focal spot to the center of the image receptor. Tube positions and angles were verified using a Digi-Pas model DWL-80G digital angle gauge (Digipas USA LLC, Avon, CT) and Kobalt LDM-35 laser distance meter (Lowe's Corp., Mooresville, NC). Radiographic automatic exposure-control (AEC) settings were average size chest AP and lateral, 120 kVp, zero added filtration.

Signal-to-noise ratio and milliampere-seconds relation

Projection mAs was computed per equation (3) using $f = 10$, 5, and 2.5. The minimum mAs setting for the generator exceeded computed values; therefore, the projection image pixel intensity was reduced and noise added to simulate computed mAs values using image processing software Fiji in the following order[25]:

$$\left(N_f\right)_{i,j} = \left(\frac{mAs\ per\ projection}{mAs_{raw}}\right) \times \left(N_{raw}\right)_{i,j}, \quad (12)$$

followed by

$$\sigma_f = \sigma_{modified} \times \sqrt{\frac{mAs_{raw}}{mAs\ per\ projection}}, \quad (13)$$

where $\left(N_f\right)_{i,j}$ are the pixel values in the projection image modified per f; $\left(N_{raw}\right)_{i,j}$ are the pixel values in the original raw projection image; $mAs\ per\ projection$ is per eq (3); mAs_{raw} is the manual mAs setting used to produce the raw projection image; σ_f is the pixel standard deviation of a region of interest (ROI) over a physically uniform section of the phantom that is inferior to the diaphragm in the final image; $\sigma_{modified}$ is the pixel standard deviation of an ROI over a uniform section of the phantom beneath the

diaphragm in the raw projection image modified per equation (12).

Image processing and reconstruction

Tomosynthesis reconstruction was done with a C++ algebraic algorithm. Noise injections and image analyses were done with Fiji.

Image analysis

Iodine SNR levels were determined as:

$$SNR = \frac{\left(ROI\ mean\right)_I - \left(ROI\ mean\right)_{Bkg}}{\left(ROI\ std.dev.\right)_{Bkg}} \quad (14)$$

where $\left(ROI\ mean\right)_I$, $\left(ROI\ mean\right)_{Bkg}$, and $\left(ROI\ std.dev.\right)_{Bkg}$ are the ROI mean values for the iodine insert and background regions and the standard deviation in ROI values in background regions, respectively. ROI locations were consistent from image to image.

Results

Technique factors

AEC radiographic, small focal-spot techniques were 120 kVp, AP projection 0.37 mAs, and lateral projection 1.28 mAs. Manual techniques per projection were 120 kVp, zero added filtration for AP and lateral projections, and 0.43 mAs, which is referred to as full mAs.

Tomosynthesis model results per equations (1) through (10) using $n = 3$ are given in Table 1. Anode currents versus breathing amplitude b at $f = 5$, bpm = 10 and 15, and $D = 0.5$ and 1 mm are presented in Figure 1 for AP and lateral views. Dependence relationships in the model are given in Table 2. Figure 2 presents scout views and DTS reconstructions.

Iodine signal-to-noise ratio comparisons

SNR results are presented in Table 3. SNR values vary in an anthropomorphic lung phantom due to anatomical noise. Generally, tomosynthesis improves SNR over a single radiograph when anatomical noise is present.

Conclusions and discussion

Imaging parameter relations are provided in Tables 1 and 2 and Figure 1. Proportional relations exist between mA and both D and bpm. Lateral imaging requires increased anode current.

Table 1   Sample technique factors required by 4-dimentional Tomo model

D (mm)	bpm	b (mm)	Projection rate (sec^{-1})	Sweep duration (msec)	Pulse duration (msec)
0.5	15	40	5862	10.41	0.161
		30	4397	13.87	0.217
		20	2931	20.81	0.331
		10	1466	41.62	0.672
	10	40	3908	15.61	0.246
		30	2931	20.81	0.331
		20	1954	31.22	0.502
		10	977	62.44	1.014
1	15	40	2931	20.81	0.331
		30	2198	27.75	0.445
		20	1466	41.62	0.672
		10	733	83.25	1.355
	10	40	1954	31.22	0.502
		30	1466	41.62	0.672
		20	977	62.44	1.014
		10	489	124.87	2.037

b, motion amplitude; bpm, breaths per minute; D, desired maximum tissue travel during the sweep.

Figure 1   A. Anterior-posterior view anode current versus breathing amplitude b at $f = 5$, bpm = 10 and 15, and $D = 0.5$ and 1 mm. B. Lateral view anode current versus breathing amplitude b at $f = 5$, bpm = 10 and 15, and $D = 0.5$ and 1 mm.

Current and pulse duration demands present engineering challenges. Current density (A/cm^2) of cold cathodes varies inversely with emitter surface area. Smith et al reported a carbon nanotube field-emission minimum pulse duration of 0.02 msec and maximum current density of 0.8 A/cm^2 from a 0.04 cm^2 surface area.[23] Schwoebel et al achieved a 300 mA current with a 0.1 msec pulse width using a 50,000 tip array Spindt-field emitter array with expectations of >1 A from the same size array.[20] Demands might be met by focusing beams from ≥2 emitters onto each focal spot.

Relative SNR was chosen to test mAs reduction. DTS SNR is also heavily dependent on anatomical noise. Projection mAs was reduced from clinical standard values using $f = 2.5$ and 5. Figures 2 and 3 and Table 3 support DTS in 3 of 4 capsule views using $f = 5$ and demonstrate that objects with SNR = 2 are visible at least in this configuration. Lateral scout AEC radiographic images show lung capsule visibility as absent but present in the DTS reconstructions.

AP behind heart DTS SNR is less than the scout AEC projection SNR at $f = 5$ and 2.5 due to the simulated noise increase at reduced mAs, which overwhelmed signal improvement provided by DTS. Generally, slice sensitivity profiles produced with DTS exhibit a nonuniform frequency response with an inverse relationship between slice profile thickness and spatial frequency.[26] The abundance of low-frequency information in the posterior portion of the heart nearest to the capsule contributed to the capsule plane. Nonuniform frequency response can be improved with refined reconstruction techniques.[26]

Ripple artifacts and poor visibility of the lateral right-lung capsule reconstructions result from a significant amount of information falling outside the detector due to projection geometry. This can be corrected by increasing the detector length in the sweep direction or distributing sources in a 2-dimensional pattern and widening the detector to ensure that an adequate number of projections is included in the reconstruction and by positioning the lateral image receptor on a unilateral lesion side.
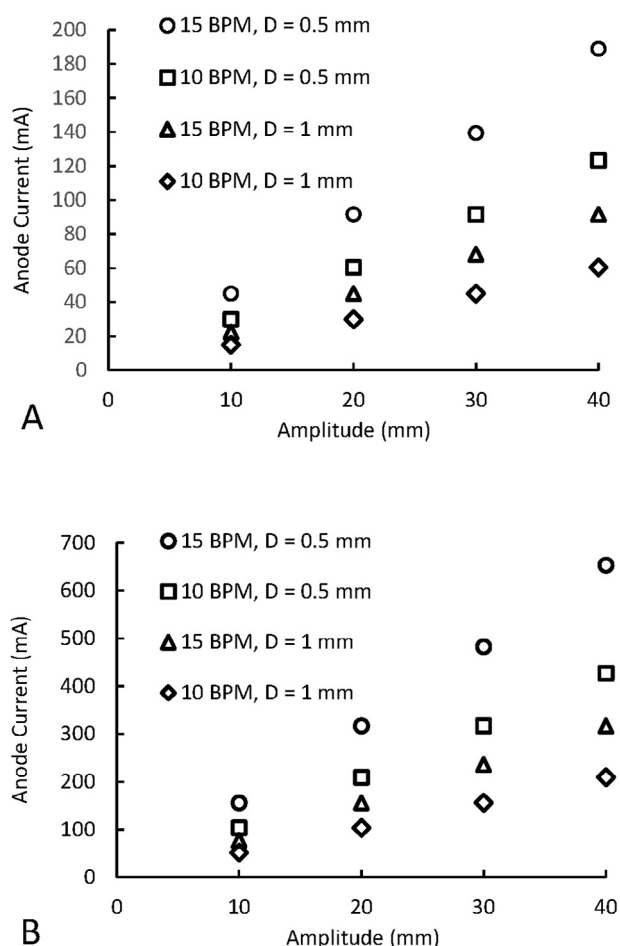
Table 2   Dependence relations among 4-dimensional Tomo model parameters

	D	b	NP	f
mAs/projection	P	IND	IP	P
Projection rate	IP	P	P	IND
Sweep duration	P	IP	IND	IND
Pulse duration	P	IP	IP	IND
mA	IP	P	IND	P

b, motion amplitude; D, desired maximum tissue travel during the sweep; f, noise-scaling factor with 10 regarded as clinically acceptable; IND, independent; IP, inversely proportional; mAs, milliampere-seconds; NP, number of projections per sweep; P, proportional.
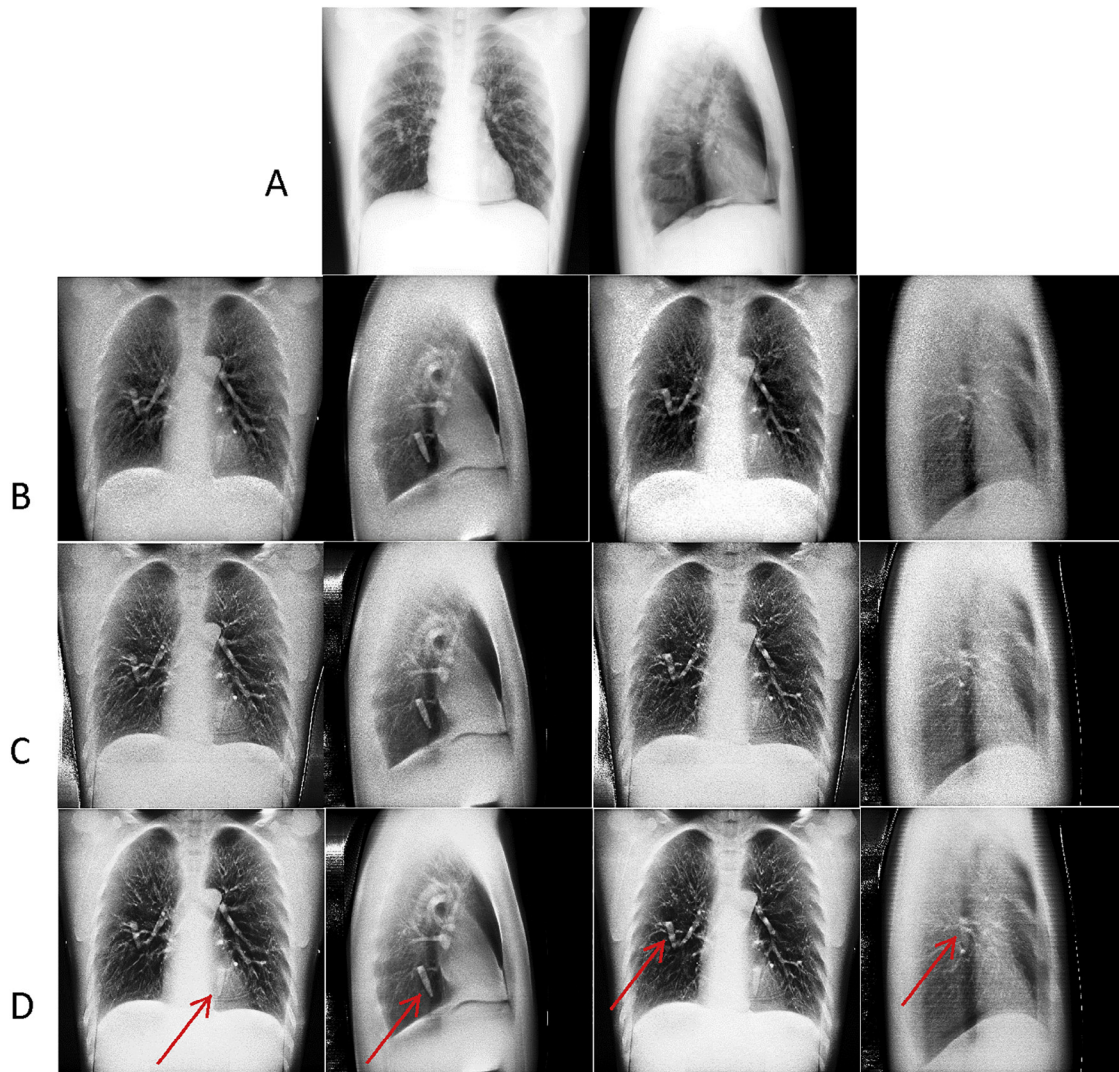
Figure 2   Row A: Anterior-posterior and lateral scout views; row B: $f = 2.5$ reconstructions; row C: $f = 5$ reconstructions; row D: $f = 10$ reconstructions. Columns left to right are capsule behind heart anterior-posterior, capsule behind the heart lateral, capsule in the right lung anterior-posterior, and capsule in the right lung lateral. Red arrows point to capsules in each orientation.

Table 3   SNR results at 3 tomosynthesis imaging mAs levels

	Lung capsule SNR	Capsule behind heart SNR
Anterior-posterior		
Tomosynthesis $f = 2.5$	3.86 ± 0.88	1.20 ± 0.44
Tomosynthesis $f = 5$	7.60 ± 0.90	2.60 ± 0.58
Tomosynthesis $f = 10$	14.11 ± 0.96	5.84 ± 0.66
Automatic exposure control	3.05 ± 0.12	3.60 ± 0.15
Lateral		
Tomosynthesis $f = 2.5$	0.73 ± 0.23	2.73 ± 0.26
Tomosynthesis $f = 5$	1.12 ± 0.22	5.65 ± 0.87
Tomosynthesis $f = 10$	1.99 ± 0.21	8.08 ± 0.74
Automatic exposure control	Not Visible	0.83 ± 0.03

mAs, milliampere-seconds; SNR, signal-to-noise ratio.

Patient-specific anatomical noise limits quality metric predictability. An appropriate approach might be mAs adjustment on the basis of relationships between a standardized phantom metric and receptor dose during scout exposures. For example, Svalkvist and Bath successfully developed a model to simulate system noise in reduced dose DTS projections on the basis of noise power spectrum and detective quantum efficiency using flat-field images at multiple projections and dose levels.[27] This could be modified to establish patient-specific mAs values as a function of image receptor dose determined during the scout. Exposure versus SNR relations might be established using a standardized phantom of variable size with appropriate test inserts.

Similarly, Li and Dobbins developed a noise power spectrum-based method to simulate reduced exposure and
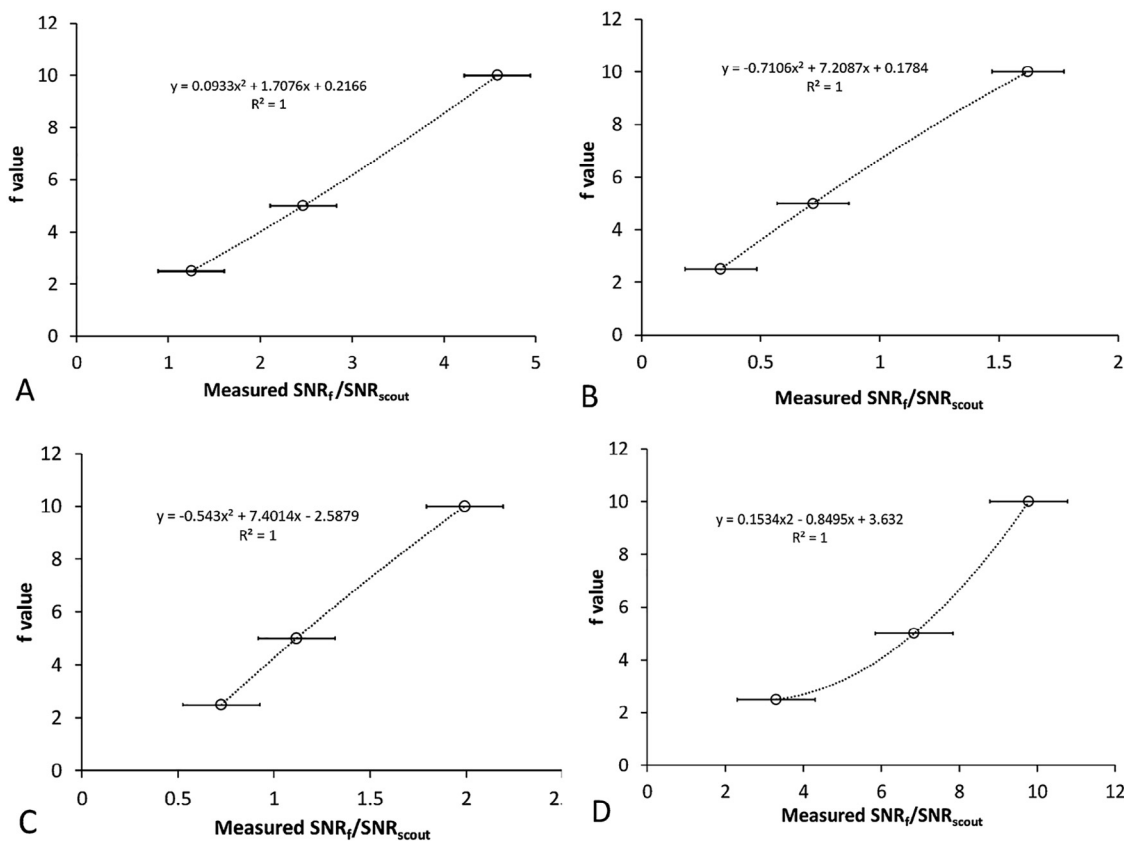
Figure 3 f versus measured signal-to-noise ratio (SNR) SNR_f/SNR_{scout} for the lung and behind heart capsules. A. Anterior-posterior lung. B. Anterior-posterior heart. C. Lateral lung. D. Lateral heart. Lateral lung SNR_{scout} is assigned the value of 1 because the capsule is inconspicuous in the scout.

measure SNR versus cumulative exposure for simulated nodules and simulated noise in clinical DTS projections but without actual reduced-dose imaging.[28]

The f versus measured $SNR_f/SNR_{(scout)}$ example could be a format to present data that are generated using the method by Svalkvist and Bath applied to a standardized phantom with inserted test objects.

Additionally, mAs per projection and mA depend on geometry, habitus, x-ray spectrum, subject contrast, and detector efficiency. mA demands may be reduced by improved detectors, reconstruction algorithms that further reduce overlying structures interference, photon counting (Radiation Monitoring Devices, Inc.), and dual-energy imaging, albeit with increased demands on mA, pulse duration, image detection, and readout.[26,29-34]

Limitations of depth resolution can be corrected by orthogonal pair imaging coupled with a Boolean combination of contours from both planes, in which case motion capture constraints are best met by simultaneous AP/lateral imaging. This might be facilitated by employing the radiographic and cone beam CT scatter correction method by Siewerdsen et al.[35]

Using the GE Definium 8000 VolumeRAD DTS system, Sabol determined an average adult male chest examination effective dose of 0.124 to 0.134 mSv, which is less than 75% of that predicted by linear scaling of the mAs ratio, using a 120 kVp spectrum, no additional filtration, and GE-recommended mAs, or noise, scaling factor of 10.[19] The reduction was due to focal-spot-to-skin-distance variations, collimation changes with projection angle, rounding down the mAs, and variations in organ exposure for each view. This approximates the effective dose of a single rapid 4-dimensional DTS phase capture. Multiple phases or orthogonal view tomosynthesis would increase the effective dose. Multiphase studies would incur a dose that is approximately equal to:

$$Effective\ Dose \cong 0.75 \times (number\ of\ phases)$$
$$\times (mAs\ scaling\ factor) \times (single\ radiograph\ dose) \quad (15)$$

Ten phases that use an mAs scaling factor of 10 produces an approximate effective dose ≤ 75 single projection radiographs.

References

1. Keall PJ, Mageras GS, Balter JM, et al. The management of respiratory motion in radiation oncology report of AAPM Task Group 76. *Med Phys*. 2006;33:3874-3900.
2. Yamamoto T, Langner U, Loo BW Jr, Shen J, Keall PJ. Retrospective analysis of artifacts in four-dimensional CT images of 50

abdominal and thoracic radiotherapy patients. *Int J Radiat Oncol Biol Phys*. 2008;72:1250-1258.

3. Dobbins JT 3rd, McAdams HP, Sabol JM, et al. Multi-institutional evaluation of digital tomosynthesis, dual-energy radiography, and conventional chest radiography for the detection and management of pulmonary nodules. *Radiology*. 2017;282:236-250.

4. Wahidi MM, Govert JA, Goudar RK, Gould MK, McCrory DC. Evidence for the treatment of patients with pulmonary nodules: When is it lung cancer?: ACCP evidence-based clinical practice guidelines. *Chest*. 2007;132:94S-107S.

5. MacMahon H, Austin JH, Gamsu G, et al. Guidelines for management of small pulmonary nodules detected on CT scans: A statement from the Fleischner Society 1. *Radiology*. 2005;237:395-400.

6. Gould MK, Fletcher J, Iannettoni MD, et al. Evaluation of patients with pulmonary nodules: When is it lung cancer?: ACCP evidence-based clinical practice guidelines. *Chest*. 2007;132:108S-130S.

7. Shan J, Tucker AW, Lee YZ, et al., eds. *Evaluation of Imaging Geometry for Stationary Chest Tomosynthesis*. Bellingham, WA: SPIE Medical Imaging; 2014.

8. Hartman AE, Shan J, Wu G, et al., eds. *Initial Clinical Evaluation of Stationary Digital Chest Tomosynthesis*. Bellingham, WA: SPIE Medical Imaging; 2016.

9. Shan J, Burk L, Wu G, et al., eds. *Prospective Gated Chest Tomosynthesis Using CNT X-Ray Source Array*. Bellingham, WA: SPIE Medical Imaging; 2015.

10. Maurer J, Godfrey D, Wang Z, Yin FF. On-board four-dimensional digital tomosynthesis: First experimental results. *Med Phys*. 2008;35:3574-3583.

11. Hsieh SS, Ng LW. Real-time tomosynthesis for radiation therapy guidance. *Med Phys*. 2017;44:5584-5595.

12. Zhang Y, Ren L, Ling CC, Yin FF. Respiration-phase-matched digital tomosynthesis imaging for moving target verification: A feasibility study. *Med Phys*. 2013;40:071723.

13. Zhang Y, Ren L, Vergalasova I, Yin FF. Clinical study of orthogonal-view phase-matched digital tomosynthesis for lung tumor localization. *Technol Cancer Res Treat*. 2017;1533034617705716.

14. Santoro J, Kriminski S, Lovelock DM, et al. Evaluation of respiration-correlated digital tomosynthesis in lung. *Med Phys*. 2010;37:1237-1245.

15. Maltz JS, Sprenger F, Fuerst J, Paidi A, Fadler F, Bani-Hashemi AR. Fixed gantry tomosynthesis system for radiation therapy image guidance based on a multiple source x-ray tube with carbon nanotube cathodes. *Med Phys*. 2009;36:1624-1636.

16. Verma P, Wu H, Langer M, Das I, Sandison G. Survey: Real-time tumor motion prediction for image-guided radiation treatment. *Comp Sci Eng*. 2011;13:24-35.

17. Harders SW, Madsen HH, Nellemann HM, et al. Dynamic contrast-enhanced CT in suspected lung cancer: Quantitative results. *Br J Radiol*. 2013;86:20130257.

18. Deller T, Jabri KN, Sabol JM, et al., eds. *Effect of Acquisition Parameters on Image Quality in Digital Tomosynthesis*. Bellingham, WA: SPIE Medical Imaging; 2007.

19. Sabol JM. A Monte Carlo estimation of effective dose in chest tomosynthesis. *Med Phys*. 2009;36:5480-5487.

20. Schwoebel PR, Boone JM, Shao J. Studies of a prototype linear stationary x-ray source for tomosynthesis imaging. *Phys Med Biol*. 2014;59:2393-2413.

21. Sprenger F, Calderon-Colon X, Cheng Y, et al. Distributed source x-ray tube technology for tomosynthesis imaging. *Proc SPIE Int Soc Opt Eng*. 2010;7622:76225M.

22. Calderon-Colon X, Geng H, Gao B, An L, Cao G, Zhou O. A carbon nanotube field emission cathode with high current density and long-term stability. *Nanotechnology*. 2009;20:325707.

23. Smith DJ, Bui PA, Michael JD, Aceto SC, Marquard K, Brewer JE, eds. *Stable, High Current Density Carbon Nanotube Field Emission Devices*. Kyoto, Japan: Vacuum Nanoelectronics; 2013.

24. Lujan AE, Balter JM, Ten Haken RK. A method for incorporating organ motion due to breathing into 3D dose calculations in the liver: Sensitivity to variations in motion. *Med Phys*. 2003;30:2643-2649.

25. Schindelin J, Arganda-Carreras I, Frise E, et al. Fiji: An open-source platform for biological-image analysis. *Nat Methods*. 2012;9:676-682.

26. Godfrey DJ, McAdams H, Dobbins IIIJT. Optimization of the matrix inversion tomosynthesis (MITS) impulse response and modulation transfer function characteristics for chest imaging. *Med Phys*. 2006;33:655-667.

27. Svalkvist A, Båth M. Simulation of dose reduction in tomosynthesis. *Med Phys*. 2010;37:258-269.

28. Li CM, Dobbins JT III, eds. *Methodology for Determining Dose Reduction for Chest Tomosynthesis*. Bellingham, WA: SPIE Medical Imaging; 2007.

29. Dobbins JT 3rd, McAdams HP. Chest tomosynthesis: Technical principles and clinical update. *Eur J Radiol*. 2009;72:244-251.

30. Weber MJ. Inorganic scintillators: Today and tomorrow. *J Luminescence*. 2002;100:35-45.

31. Nikl M. Scintillation detectors for x-rays. *Measure Sci Technol*. 2006;17:R37.

32. Cha BK, Lee SJ, Muralidharan P, Kim JY, Kim DK, Cho G. Characterization and imaging performance of nanoscintillator screen for high resolution X-ray imaging detectors. *Nucl Instr Methods Phys Res*. 2011;633:S294-S296.

33. van Eijk CW. Inorganic scintillators in medical imaging. *Phys Med Biol*. 2002;47:R85-R106.

34. Shkumat NA, Siewerdsen JH, Dhanantwari AC, et al. Optimization of image acquisition techniques for dual-energy imaging of the chest. *Med Phys*. 2007;34:3904-3915.

35. Siewerdsen J, Daly M, Bakhtiar B, et al. A simple, direct method for x-ray scatter estimation and correction in digital radiography and cone-beam CT. *Med Phys*. 2006;33:187-197.